NeuroImage **17,** 47–60 (2002)
doi:10.1006/nimg.2002.1152

Wavelet-Aided Parametric Mapping of Cerebral Dopamine D_2 Receptors Using the High Affinity PET Radioligand [^{11}C]FLB 457

Zsolt Cselényi,* Hans Olsson,* Lars Farde,* and Balázs Gulyás*,†

**Karolinska Institutet, Department of Clinical Neuroscience, Psychiatry Section, Karolinska Hospital, S-171 76 Stockholm, Sweden; and †Department of Neuroscience, Karolinska Institutet, S-171 77 Stockholm, Sweden*

Received November 20, 2001

The study of human neuroreceptor systems by means of positron emission tomography (PET) and suitable radioligands has proven to be of great importance in research on normal brain functions and the pathophysiology and treatment of neuropsychiatric disorders. A for long identified goal is to produce detailed parametric maps of showing neuroreceptor binding parameters for the entire human brain *in vivo*. The application of wavelet filters has recently been proposed as a solution to handle the inherently low signal-to-noise ratio of PET images. In the present study we applied the wavelet approach to data obtained from 10 healthy subjects who were examined with [^{11}C]FLB 457. This high affinity dopamine D_2-receptor antagonist provides a signal from a range of regions with a hundredfold difference in receptor density and should thus be suitable for evaluation of the wavelet approach. For cross-validation purposes the data were analysed with four methods: a traditional region-of-interest (ROI) based analysis, a pixel-based analysis and two variants of wavelet-aided analyses. In both variants the wavelet filter was spatially applied, but a two-dimensional filter was used in one case and a three-dimensional one in the other. The same linear-graphical binding potential (BP) estimation step was used for all methods and the results of the three parametric mapping techniques were compared to the reference ROI-based method by calculating the average BP of representative ROIs. The pixel-based and the two-dimensional-wavelet-based methods yielded highly correlated but systematically lower values when compared to the reference ROI-based method. The approach utilising three-dimensional wavelet filters yielded BP maps with regional averages closely matching the values of the ROI-based method. The results show that the combination of three-dimensional spatial wavelet filtering with established parameter estimation procedures provides detailed, accurate maps of radioligand binding parameters. Such maps can be used for in inter-individual or multi-condition comparisons of binding parameters at subregional levels.

INTRODUCTION

Brain imaging of neurotransmission systems has a central role in research on normal brain functions as well as on the pathophysiology and treatment of neuropsychiatric disorders. A multitude of neuroreceptors is expressed in the human brain. Each neuroreceptor has a distinct anatomical distribution and the density of any given type varies greatly among regions. Moreover, the density also varies between individuals and it may be changed in relation to disease conditions (Farde *et al.,* 1995). There is thus a need for accurate and precise quantification of neuroreceptor binding over a wide density range.

Positron Emission Tomography (PET) and Single Photon Emission Tomography (SPET) are used to trace radioactivity after intravenous injection of a radioligand that binds to central neuroreceptors. Radioligand binding is often described by biological parameters, which are obtained by kinetic analyses of regional time-activity curves (TAC's) (Farde *et al.,* 1989; Blomqvist, 1991; Drevets *et al.,* 1999; Olsson *et al.,* 1999; Abi-Dargham *et al.,* 2000). Most quantitative approaches are based on analysis of average radioactivity in regions of interest (ROIs) or volumes of interest (VOIs) (Farde *et al.,* 1989; Koeppe *et al.,* 1996; Ito *et al.,* 1998; Zubieta *et al.,* 1998; Olsson *et al.,* 1999; Kaasinen *et al.,* 2001). The ROIs or VOIs are identified manually or by templates on the individual functional images (Abadie *et al.,* 1992; Madar *et al.,* 1996; Smith *et al.,* 1998; Drevets *et al.,* 1999; Abi-Dargham *et al.,* 2000). A ROI-based analysis provides an estimate for the average value in a region. However, neuroreceptors may be heterogeneously distributed within a region and information regarding subregional differences may consequently be lost.

In order to obtain more detailed information about receptor distribution several attempts have been made to apply the kinetic calculations to individual pixel (or more precisely voxel) data. The generated distribution map is often referred to as a parametric image (Blomqvist *et al.,* 1990; Frey *et al.,* 1991; Gunn *et al.,*

1053-8119/02 $35.00

1997). Due to large computational demands of this approach it is common to use linear graphical algorithms since they allow for rapid calculations of binding parameters. Estimation of the binding potential (BP) by graphical approaches has, however, been demonstrated to be greatly affected by noise in the time-activity curves (Abi-Dargham *et al.*, 2000; Slifstein and Laruelle, 2000). The higher the noise is the lower the estimated BP value will be when compared to the BP for the noise-free signals.

The use of wavelet filters is a new approach for pixel-based analysis (Turkheimer *et al.*, 1999; Millet *et al.*, 2000a; Millet *et al.*, 2000b; Turkheimer *et al.*, 2000a; Turkheimer *et al.*, 2000b). This technique allows for the identification of signal patterns thereby differentiating signal from noise in the original sample. In PET studies on radioligand binding it means that the spatiotemporal patterns can be analysed to obtain a *whole map* of receptor density in contrast with the traditional ROI-based methods that produce *one number per region* only. These works establish the basic principles of working with wavelets in the context of analysing neuroreceptor imaging.

[^{11}C]FLB 457 is a new radioligand with very high affinity for D_2/D_3 dopamine receptors (Halldin *et al.*, 1995; Farde *et al.*, 1997). Due to its high affinity, [^{11}C]FLB 457 can be used to demonstrate binding even in regions with a low density of receptors (Farde *et al.*, 1997; Okubo *et al.*, 1999; Olsson *et al.*, 1999; Suhara *et al.*, 2001). Signals from a range of regions with a 100-fold difference in D_2-receptor density makes [^{11}C]FLB 457 particularly suitable for a critical examination of the recently proposed wavelet-based analysis.

Building upon these proposed techniques, the aim of the present study is to assess the capability of wavelet-aided framework to decrease to noise-sensitivity of a parameter estimation procedure. For that reason four methods, built on the same linear-graphical parameter estimation step, were compared for cross validation purposes; a traditional ROI-based analysis, a pixel-based analysis and two variants of wavelet-aided analyses. In both variants the wavelet transform is applied spatially. The difference is whether it is applied two dimensionally to each slice of the volume or three dimensionally to the whole volume. The results of the ROI-based approach served as a reference for evaluation of the other three methods. The calculations were performed on a dataset of 10 control subjects previously examined with [^{11}C]FLB 457.

METHODS

Wavelets in Theory

The wavelet analysis of signals resembles the better-known Fourier analysis. In case of either technique the signal can be one-dimensional, such as a temporal sample of a sound wave, or two- or three-dimensional such as a two- or three-dimensional image. According to the Fourier theorem any function or signal can be made up by the superposition of a set of sinusoids with properly chosen amplitudes and phases. To put it in a different way, the Fourier transform allows for the description of a given signal in the frequency domain by extracting the different frequency components of the signal. However, it is not able to detect the location of non-stationary or transient components within the sample. Because of this a Fourier transform of an image, which contains a great number of transient components such as edges or boundaries, is not easily suitable for localisation of spatial features.

Wavelets, in essence, resemble sinusoids but restricted to a compact, bell-shaped envelope. This restricted nature of wavelets enables them, by contrast to Fourier sinusoids, to detect patterns in both the frequency and time domains or, alternatively, both the frequency and space domains. Therefore a coefficient of a wavelet transform is a quantity describing the signal at a certain location with a certain scale ("spatial frequency") (Mallat, 1989; Daubechies, 1992; Meyer, 1992; Turkheimer *et al.*, 1999). Importantly because of this property the wavelet transform is capable of separating signal components (lower frequency) from noise (higher frequency) as the components show up in different coefficients of the transform.

Another property of the wavelet transform is that if the signal is well "lined-up" with the wavelet filter then the transform "accumulates" the signal in a few large coefficients whereas the noise is spread in a large number of small coefficients. This is advantageous in most of the applications of wavelets as small coefficients can be safely disregarded without the loss of the information content of the signal.

From the viewpoint of noise reduction these two properties mean that the "noise" coefficients are not only separate but also they can be identified and deleted because of their low value.

Furthermore, the wavelet transform is a linear operator and thus, if applied spatially on each timeframe of a four-dimensional radioligand study, the original temporal kinetics of the radiotracer is left undisturbed (Turkheimer *et al.*, 2000a). In other words a kinetically homogenous region of the brain, such as a high receptor density structure with a distinct time–activity curve, will be represented with a wavelet coefficient that exhibits a time–activity curve with the same characteristics. On the other hand noise "patterns" give rise to coefficients that do not show any comprehensible temporal relationships. Noise can thus be identified and deleted when the kinetic analysis is initiated.

Wavelets in Practice

The wavelet transform used in the present study is realised through an iterative decomposition algorithm

known as the dyadic discrete wavelet transform (dyadic DWT), which is described in detail in the literature (Mallat, 1989; Unser *et al.*, 1995; Turkheimer *et al.*, 1999). The following represents a schematic overview of the wavelet algorithm. Initially we describe decomposition in one dimension (Fig. 1a) and then the reconstruction procedure (Fig. 1b).

1. Convolution. The data is passed through a low- and a highpass filter (called wavelet filters) by convolving with the wavelet filter *kernels*. The low pass part or *subband* is called *approximations* (low frequency components of the signal), the highpass part is called *details*.

2. Downsampling. A downsampling is then performed, since the amount of information is duplicated in the first step. This means that every second coefficient of the *approximations* and *details* is thrown away. The downsampling introduces distortions that are called *aliasing* distortions. They are "cancelled out" during the reconstruction of the signal.

3. Iterative repetition. The first and second steps are repeated, always using the downscaled output of the lowpass filter (*approximations*) as input for the next iteration or next level. The *details* coefficients are kept, whereas the *approximations* are replaced with the output of the last iteration. Finally, there is one *approximations* and as many *details* as the number of iterations. The number of iterations is referred to as the *depth* of the decomposition. Due to the fact that the output is always downsampled at each level but the wavelet filters are the same, the cut-off frequency for the low- and highpass filtering steps is always lower and lower. Thus the final *approximations* part accumulates the lowest frequency components of the input sample. In other words the higher the depth the lower is the frequency of the lowest-frequency pattern extracted in the (*approximations*) coefficients.

The reconstruction procedure is basically the inverted version of decomposition (Fig. 1b):

1. Upsampling. The *approximations* and the *details* of the deepest level are upsampled. This means that zeros are inserted between every coefficient. This is to compensate for the downsampling step of the decomposition.

2. Convolution. The upsampled subbands are convolved with reconstruction low- and highpass filters, respectively. These reconstruction filters are close relatives of the decomposition filters, but not identical since the reconstruction filters must compensate for the aforementioned aliasing distortions.

3. Summation. The output of the two filters is summed to yield the reconstructed *approximations* for the next level. As we mentioned this subband was deleted during decomposition.

4. Iterative repetition. The procedure is repeated using the freshly reconstructed *approximations* and the corresponding *details* of the next level. At the coarsest level we end up with the reconstructed sample (which is an approximation of the original sample).

The procedure can be applied to two- and higher-dimensional (spatial) samples resulting in two- or higher-dimensional wavelet decompositions (Figs. 2 and 3). If employed in two dimensions, i.e., on an image, the low- and highpass filters have to be applied sequentially. They are first applied in the first dimension, on the rows of the image, resulting in two row-filtered images. Then they are applied in the second dimension, on the columns of both row-filtered images, leading to four two-dimensionally filtered *subbands* or *quadrants*. These quadrants can be visualised in a two-by-two *grid* (Fig. 2). One quadrant comes from the application of the lowpass filter on both the rows and the columns. This corresponds to the approximations part of a one-dimensional transform. Two quadrants come from the application of both the low- and the highpass filters. The difference between the two quadrants is whether the lowpass filter was applied on the rows of the image and the highpass on the columns or vice versa. They are also called the *vertical* and *horizontal* details, which corresponds to their placement in the grid. The final quadrant is the output of the application of the highpass filter on both the rows and the columns. It is also called the *diagonal* details. The input of the next level is again the *approximations* part or quadrant.

The method can be extended to three-dimensional samples, such as each three-dimensional timeframe of a PET study. In this case the output at each level contains eight subbands or "cubes" of coefficients corresponding to the number of permutations by which the low- and highpass filters are applied to the three dimensions separately (Fig. 3). Theoretically the procedure can be applied for any n-dimensional samples always yielding 2^n subbands of coefficients at each level.

The essential component of the procedure is the specific wavelet filter used for the transform. There are many families of wavelets, each having its own characteristics such as different filter lengths corresponding to different spatial (and frequency) detection properties. According to previous works, the wavelets best suited for analysis of emission tomographic images belong to the family of orthogonal spline wavelets, more precisely the so-called Battle–Lemarie wavelets (Battle, 1987; Lemarie, 1988; Turkheimer *et al.*, 1999, and references therein).

A drawback of the traditional dyadic wavelet algorithm is that low-quality or noisy inputs can be distorted by the downsampling step to a higher extent than what the reconstruction filters can compensate for. This means that the reconstructed sample will contain artefacts. These artefacts are more likely to appear if an essential coefficient for the representation

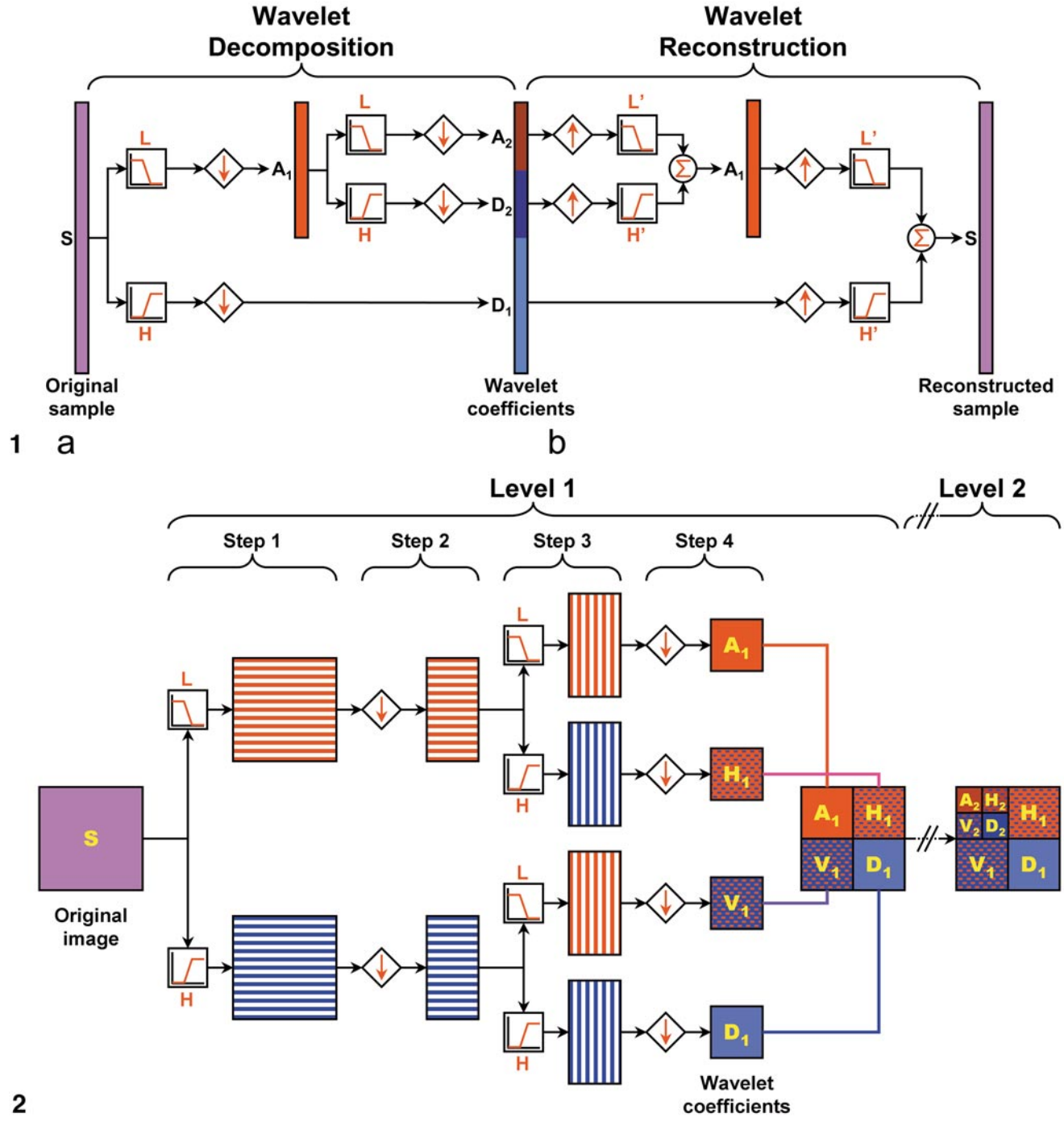

FIG. 1. Schematic diagram of the dyadic wavelet transform in one dimension. (a) Decomposition of signal with two iterations (depth two). (b) Reconstruction of signal using inverse discrete wavelet transform with two iterations. Colored bars represent the signal and the decomposition structures; S, original or reconstructed signal, A_1, approximations on the first level; A_2, approximations on the second level; D_1, details on the first level; D_2, details on the second level. The color in general symbolizes the frequency distribution of the sample from the intuitive association of low frequency with red and high frequency with blue. Therefore the original signal, which is a mixture of low and high frequencies, is represented by purple, i.e., mixture of blue and red. The color of lowpass filtered samples is red; that of highpass filtered ones is blue. Darker colors represent deeper level of decomposition. The symbol with an "L" above stands for the decomposition lowpass filtering step, the symbol with an "H" below for the decomposition highpass filtering step. Similarly the symbols with "L" and "H" represent reconstruction low- and highpass filtering, respectively. The diamond shapes with a downward or upward arrow represent decomposition downsampling and reconstruction upsampling, respectively. Finally, the round shape with a Greek capital sigma stands for the summation step of the reconstruction algorithm.

FIG. 2. Schematic diagram of the dyadic wavelet transform in two dimensions. S, signal; A, approximations; H, horizontal details; V, vertical details; and D, diagonal details. Horizontal hatching symbolizes convolution along the rows of the input, vertical hatching convolution along the columns. For details on other symbols and coloring see legend of Fig. 1.

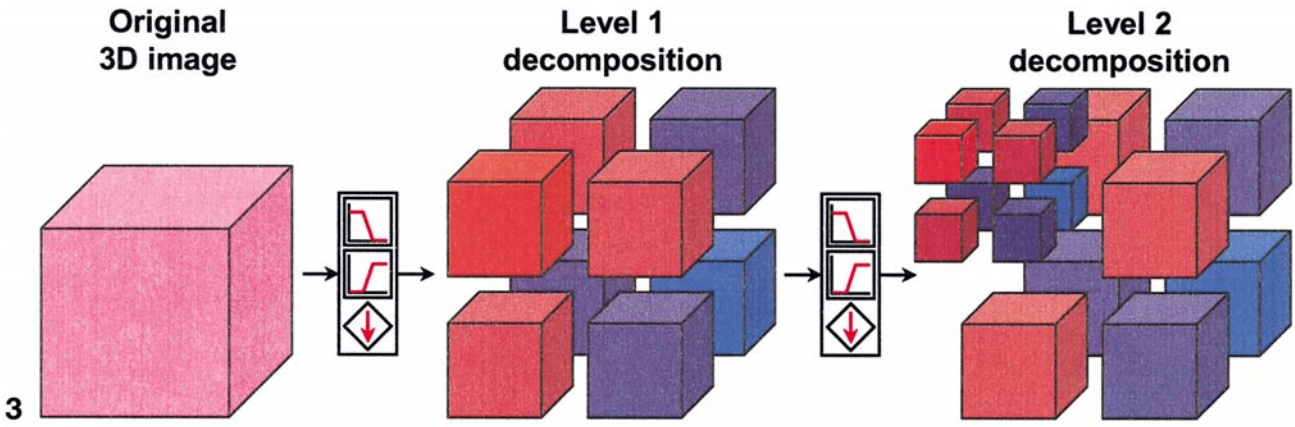

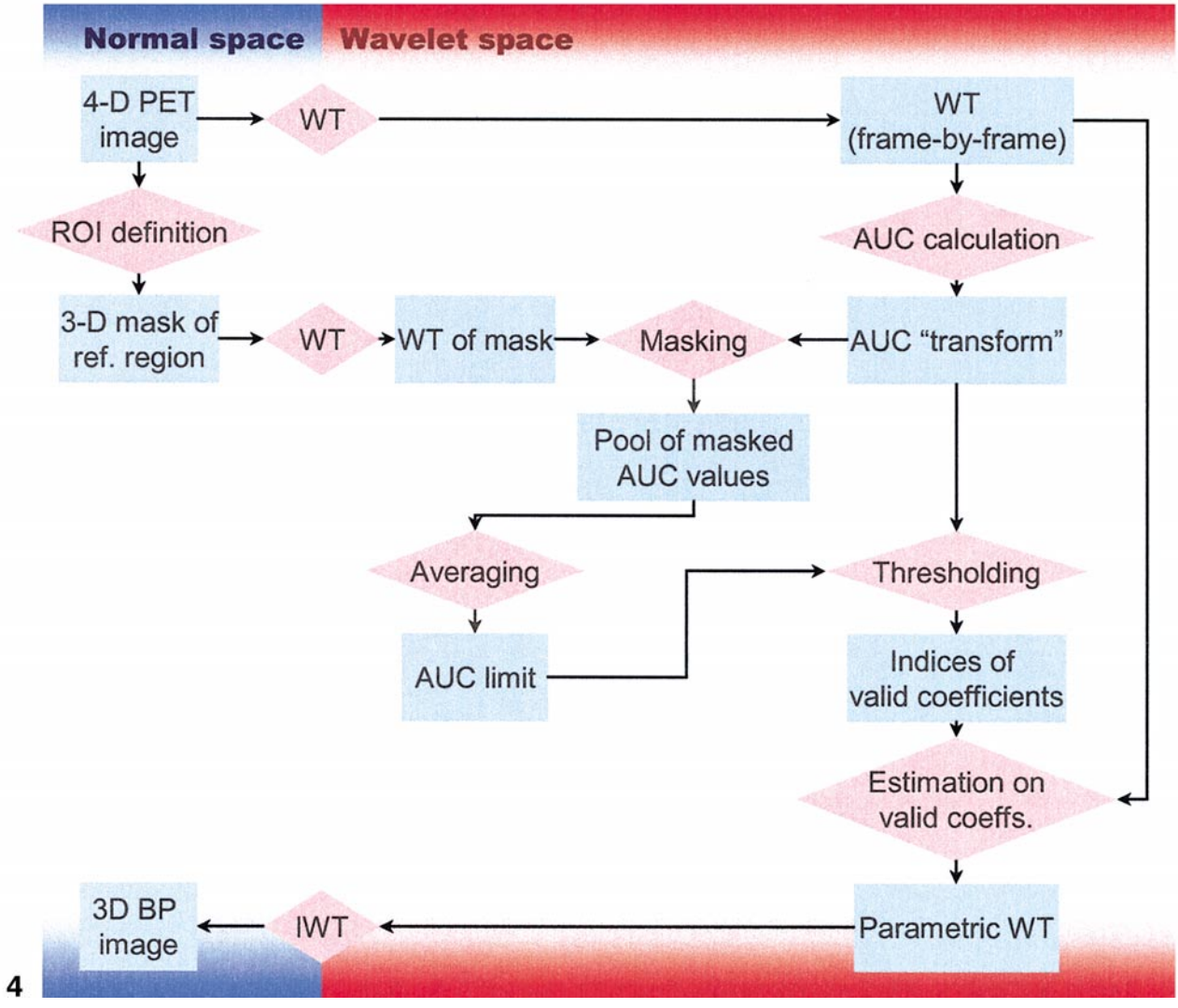

FIG. 3. Schematic visualization of decomposition structures for the three-dimensional wavelet transform. For details on symbols and coloring see legend of Fig. 1.

FIG. 4. Flowchart of the wavelet-aided binding potential estimation procedure. Blue rectangles symbolize data; pink rhombi represent procedural steps in the calculations.

of the signal was deleted during the downsampling. The presence of the artefact will be the result of a particular "constellation" of the signal and the data-points that were deleted during downsampling. As a consequence if the input is shifted by one data-point and the decomposition is performed again then the artefacts may disappear in certain locations of the sample (but others could at the same time appear in different locations).

There is a special version of the dyadic wavelet transform, which is free from this limitation. This is often referred to as the property of *translation-invariance*. In case of the three-dimensional transform, however, the translation-invariant approach is not workable at present due to the highly increased computational and storage requirements. On the other hand it has been shown that the three-dimensional wavelet transform, by utilising information in all the three principal axes, highly compensates for the lack of *translation-invariance* with regard to the quality of the decomposition (Turkheimer *et al.*, 2000b). Also the depth of the decomposition and the length of the wavelet filter kernel have great impact on the computational load. Bigger decomposition depths and longer filter kernels imply higher computational requirements. This means that a practical trade-off has to be made between quality and performance. A realistic hardware configuration contains approximately 1 gigabyte main system memory and at least a Pentium III class processor or alike.

Subjects

The subjects and imaging procedure have been described in detail earlier in a report on quantification of [^{11}C]FLB 457 binding (Olsson *et al.*, 1999). In short, the study was approved by the Ethics and Radiation Safety Committee of the Karolinska Hospital. Ten healthy male subjects, aged 23 to 38 years were enrolled and informed consent was obtained in line with the Declaration of Helsinki. The subjects were healthy according to history, medical examination, blood and urine screening tests and magnetic resonance imaging (MRI) of the brain. None of them were taking medications.

Magnetic Resonance Imaging

The MR system used was GE Sigma, 1.5 Tesla. Proton density and T_2-weighted images were obtained for all subjects. Subjects had an individual plastic helmet that kept the head in a fixed position during data acquisition (Bergström *et al.*, 1981).

Positron Emission Tomography

The PET system used was a Siemens ECAT Exact HR machine, which provides 47 slices with a center-to-center distance of 3.125 mm. The intrinsic spatial resolution is 3.6 mm in plain at the centre of the field of view and 4.0 mm full width at half maximum (FWHM) axially (Wienhard *et al.*, 1994).

The same head fixation system as in the MRI measurement was used in PET to yield the same positioning of the head in both modalities. [^{11}C]FLB 457 was prepared as previously described (Halldin *et al.*, 1995). The radioligand was injected as a bolus (t = 2 s duration) into the right cubital vein. The specific radioactivity was 1081–2086 Ci/mmol at time of injection. Total injected radioactivity was 189–299 MBq, which corresponds to an injected mass of 1.1 to 2.1 μg. After the injection the cannula was promptly flushed with 8 ml saline. After injection of [^{11}C]FLB 457 data were acquired for 63 min in consecutive time frames. The frame sequence consisted of three 1-min frames, four 3-min frames, and finally eight 6-min frames. The images were reconstructed using filtered back-projection with a Hanning filter with a cut-off frequency 0.5 of maximum, providing an in-plane resolution of 5.5 mm FWHM. Image matrix size was 128 $\times$ 128 and pixel size was 2.0 mm. Scatter correction was performed as described in the literature (Wienhard *et al.*, 1994). Attenuation correction was performed using a transmission scan obtained for each individual.

General Strategy of Calculations

Each of the individual datasets was analysed by four methods for cross-validation purposes; traditional ROI-based graphical parameter estimation, linear graphical pixel-by-pixel analysis (parametric imaging) and two types of wavelet-aided analyses. In both types the wavelet transform is applied spatially. The difference is whether it is applied two dimensionally to each slice of the volume or three dimensionally to the whole volume. The results of the ROI-based approach served as a reference for the evaluation of the other three methods.

Calculation of Binding Potential via ROI-Based Analysis

Images were transformed into standard anatomical space using the computerized human brain atlas (HBA) (Roland *et al.*, 1994). ROI's from the anatomical database of this system were positioned for 10 brain structures: the caudate nucleus, the putamen, the thalamus, the frontal cortex, the anterior and posterior cingulate cortex, the temporal cortex, the parietal cortex, the occipital cortex, the substantia nigra, and the cerebellar cortex. The cerebellar cortex was used as a reference region for free and nonspecifically bound [^{11}C]FLB 457 in brain.

The binding potential of [^{11}C]FLB 457 was estimated using the reference region version of Logan's graphical analysis (Logan *et al.*, 1996). The equation for this plot is:

$$\frac{\int_0^t C_i(t)\,dt}{C_i(t)} = \mathrm{DVR} \times \frac{\int_0^t C_{ref}(t)\,dt}{C_i(t)} + c \qquad (1)$$

where $C_i(t)$ is the TAC of the ROI, $C_{ref}(t)$ is the time activity of the reference region, DVR is the distribution volume ratio of the ligand and c is a constant.

For extrastriatal regions the curves were linear in the interval from 36 to 60 min (Olsson *et al.,* 1999). DVR was determined by fitting a line to the linear part of the plot (corresponding to the last four data-points), and the binding potential (BP) was calculated as DVR minus one.

Parametric Imaging of Binding Potential Using Pixel-by-Pixel Analysis

The procedure using Eq (1) for calculation of the binding potential was also applied for a pixel-wise analysis of the datasets. To reduce the number of calculations the fitting was not applied to pixels that have total accumulated radioactivity below a certain threshold. The accumulated radioactivity of a pixel was calculated as area under the curve (AUC) of the corresponding TAC, and the threshold is defined as the mean AUC of the cerebellar cortex because any pixel that accumulates less radioactivity than the reference tissue can be safely assumed to represent an area devoid of receptors. In addition, fitting was not applied to pixels that would yield zero divisions because of zero radioactivity values.

The AUC was used with the assumption that in those locations where the radioligand is not present or accumulates only in the initial circulatory part of the experiment it will be a value close to zero. These pixels were assumed to be part of the background or nongrey matter tissues, or completely corrupted by noise and therefore the BP at those locations was set to zero. Preliminary tests have confirmed that the assumption is correct and a BP of zero is a good approximation of the estimated BP of subthreshold locations. The final product of the calculations is a parametric image of the subject's distribution and density of dopamine D_2 receptors in brain.

The anatomical standardisation procedure using HBA was performed on the parametric images. In this way no unnecessary sources of error were introduced before the kinetic calculations. For standardisation the same warping transformations were used for each individual as in case of the ROI-based analysis. Having the images in standard space the same ROIs could be applied to determine the average binding potential of the target anatomical structures for cross-validation purposes.

Parametric Mapping of [^{11}C]FLB 457 Binding Potential Using Wavelet-Based Signal Estimation

The estimation procedure was a modification of that recently described in the literature by Turkheimer (Turkheimer *et al.,* 2000a). The flowchart of the procedure is shown in Fig. 4. The original images were transformed frame-by-frame to wavelet space using two approaches. Either the two-dimensional translation-invariant (2-DTI) or the three-dimensional (3-DWT) wavelet transform was applied. The filters for the transform belong to the Battle–Lemarie wavelets (Battle, 1987; Lemarie, 1988). The depth of the decomposition was 2 and the length of the filter kernels was 22. The parameters were chosen in an iterative approach, which yielded the best recovery of regional BP values as well as the lowest computational load.

Please note that when referring to a "coefficient" in this paragraph we should always in fact think of a temporal sequence of coefficients with the same position in the consecutive 2-D or 3-D wavelet transforms (similarly to a temporal sequence of voxels with the same spatial location in the original PET study). The coefficients of the resulting dynamic wavelet transform were analysed quantitatively in the same manner as in case of the pixel-based approach. The only difference was that a different strategy was required to determine the value for the thresholding step that was used to reduce the number of calculations. The mean AUC value of the reference region cannot be used as threshold in wavelet space as it is calculated on data in "normal" space. Therefore a 3-D mask image of the reference region (cerebellar cortex) was first created and transformed to wavelet space. Besides, the frame-by-frame transform of the input PET image was processed by calculating the frame-by-frame AUC of each coefficient. This AUC "transform" was then masked with the previously created WT of the 3-D mask to yield the AUC value of those coefficients that correspond to the reference region in normal space. The average value of this pool of AUC values was used as the thresholding limit. The thresholding step identified all valid coefficients. The parameter estimation was performed only on the valid coefficients. The end product of the calculations was a parametric wavelet transform describing the distribution of the binding potential. In the next step wavelet reconstruction was applied on the parametric transform to yield the 3-D parametric map of binding potential values in normal space.

Finally, for cross-validation purposes, anatomical standardisation and ROI based target structure analyses were performed on the parametric images in the same way as described above.

The parametric imaging calculations were performed on a PC (1.5 GHz Intel Pentium 4 processor) in Linux using Matlab (The Mathworks Inc., Natick, MA).

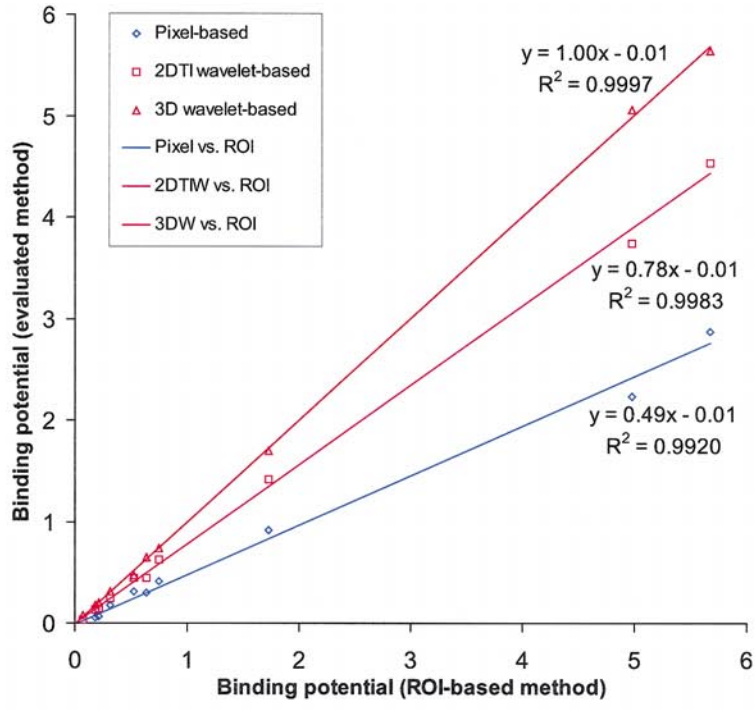
Pixel-based
2DTI wavelet-based
3D wavelet-based
Pixel vs. ROI
2DTIW vs. ROI
3DW vs. ROI
y = 1.00x - 0.01
R2 = 0.9997
y = 0.78x - 0.01
R2 = 0.9983
y = 0.49x - 0.01
R2 = 0.9920
Binding potential (evaluated method)
Binding potential (ROI-based method)
0
1
2
3
4
5
6

5

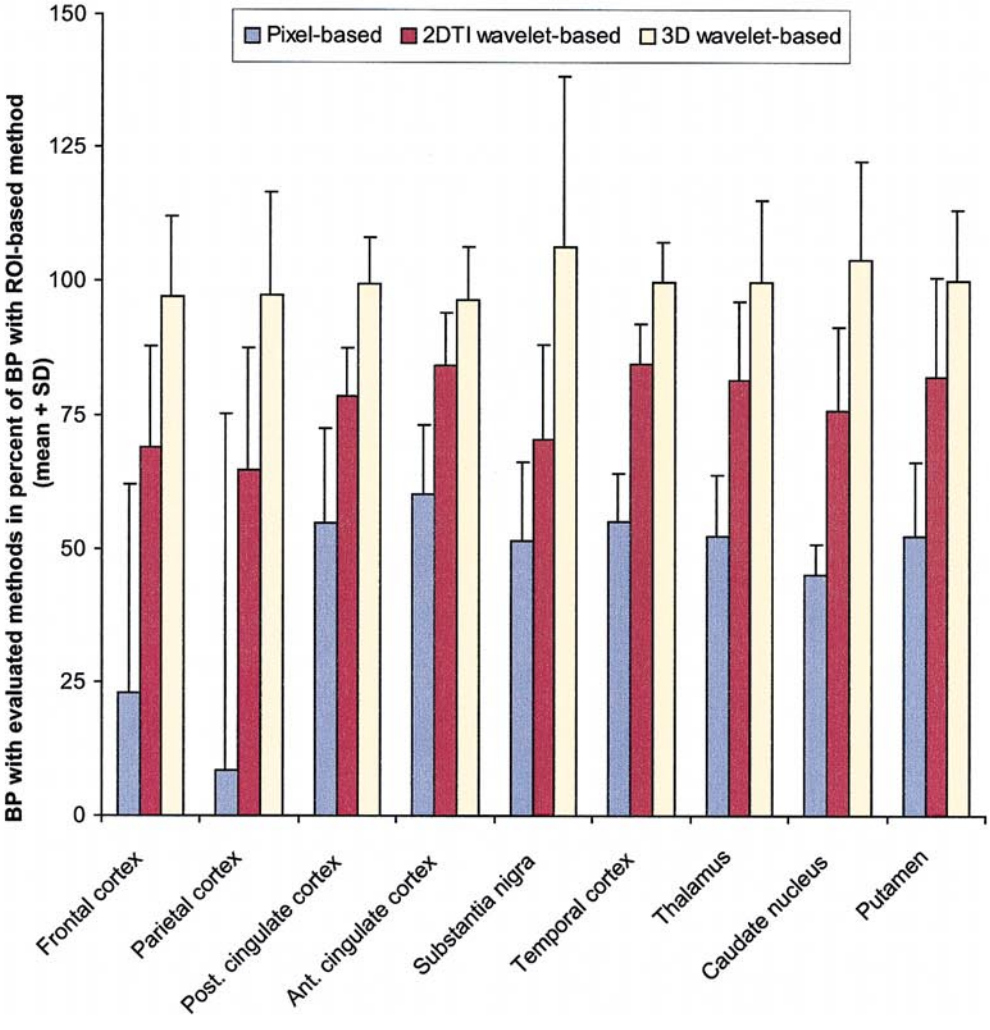
Pixel-based
2DTI wavelet-based
3D wavelet-based
BP with evaluated methods in percent of BP with ROI-based method (mean + SD)
0
25
50
75
100
125
150
Frontal cortex
Parietal cortex
Post. cingulate cortex
Ant. cingulate cortex
Substantia nigra
Temporal cortex
Thalamus
Caudate nucleus
Putamen

6

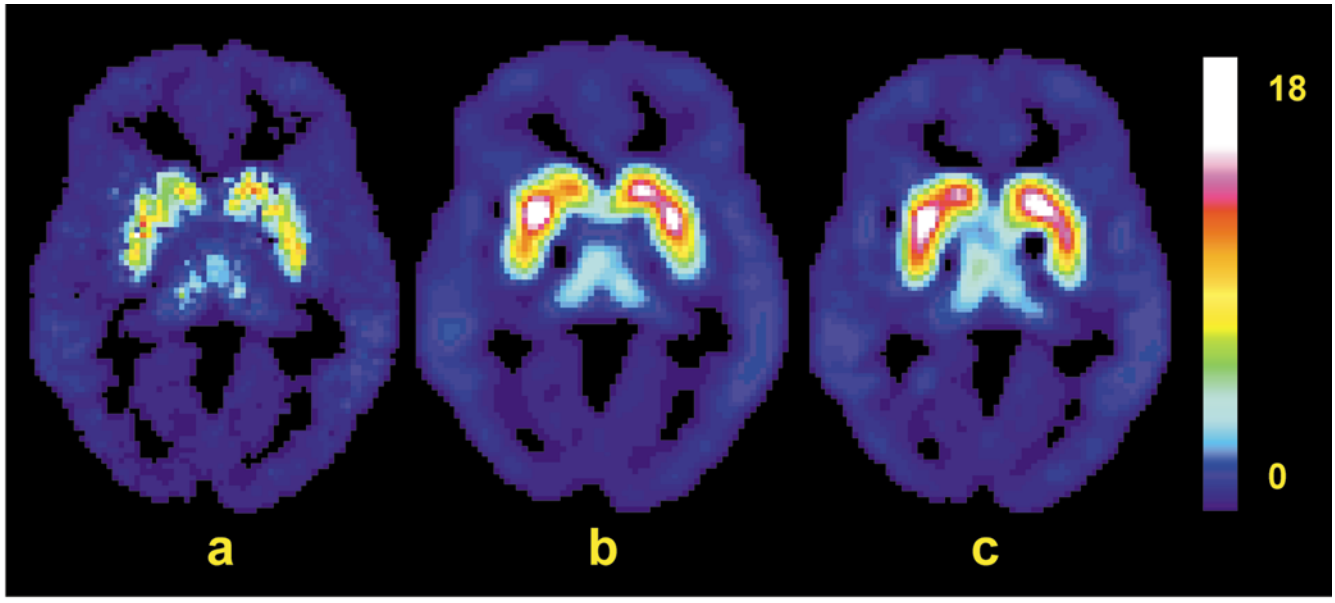

7

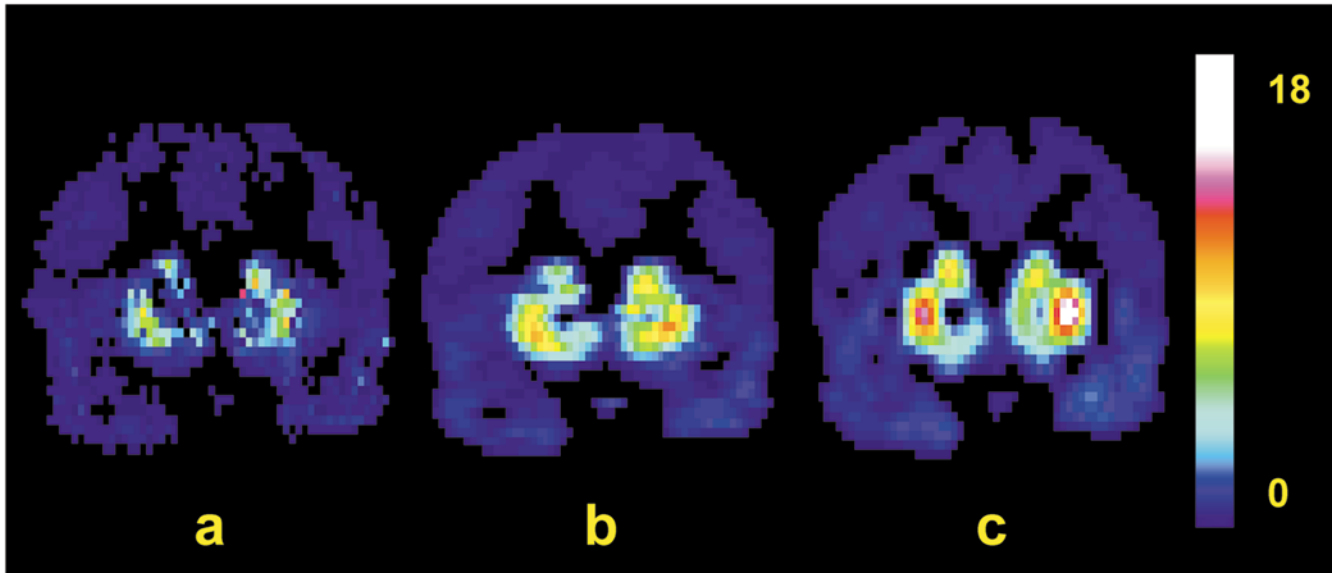

8

FIG. 7. Horizontal sections of dopamine D_2-receptor binding potential images of brain with the three parametric imaging methods. The images were obtained from the analysis of the [^{11}C]FLB 457 PET image of one of the healthy subjects of the study. The sections are showing the midlevel of the brain with the thalamus, the striatum, the frontal cortex, the parietal cortex, and the occipital cortex in view. (a) Pixel-based approach. (b) 2DTI wavelet-based approach. (c) 3-D wavelet aided approach.

FIG. 8. Coronal section of dopamine D_2-receptor binding potential images with the three parametric imaging methods. The sections are displaying the striatum, the temporal cortex, the parietal cortex, and the hypophysis. (a) Pixel-based approach. (b) 2DTI wavelet-based approach. (c) 3-D wavelet aided approach.

The software engine for the 3-D wavelet decomposition and reconstruction was originally developed in C++ by one of the authors (ZC). The final parametric images and the original PET images were transformed to a Silicon Graphics O2 workstation (Silicon Graphics, Mountain View, CA) to perform spatial standardization, ROI-fitting and ROI-based calculations. Extracted regional, per method binding potential values

FIG. 5. Regression analysis of three methods against the reference method (ROI-based analysis). Data points are mean regional binding potential values of the 10 subjects tested.

FIG. 6. Estimated regional binding potential values of the three parametric image methods in percentage of the corresponding value of the reference method (mean + SD for the 10 subjects tested).

TABLE 1

Estimated Binding Potential in Different ROIs of the 10 Subjects Tested with Four Methods (Mean ± SD)

	Methods			
Regions of interest	ROI-based	Pixel-based	2DTI wavelet-based	3-D wavelet-based
Cerebellum	−0.18 ± 0.11	−0.20 ± 0.10	−0.18 ± 0.11	−0.17 ± 0.11
Occipital cortex	0.07 ± 0.14	−0.02 ± 0.13	0.04 ± 0.15	0.07 ± 0.15
Frontal cortex	0.18 ± 0.18	0.05 ± 0.17	0.13 ± 0.18	0.18 ± 0.19
Parietal cortex	0.21 ± 0.18	0.06 ± 0.16	0.15 ± 0.18	0.20 ± 0.19
Post. cingulate cortex	0.31 ± 0.21	0.17 ± 0.18	0.24 ± 0.20	0.31 ± 0.21
Ant. cingulate cortex	0.53 ± 0.25	0.32 ± 0.22	0.44 ± 0.25	0.47 ± 0.27
Substantia nigra	0.64 ± 0.33	0.30 ± 0.18	0.45 ± 0.26	0.65 ± 0.32
Temporal cortex	0.75 ± 0.30	0.41 ± 0.25	0.63 ± 0.30	0.74 ± 0.31
Thalamus	1.73 ± 0.53	0.92 ± 0.38	1.42 ± 0.54	1.70 ± 0.54
Caudate nucleus	4.98 ± 1.68	2.23 ± 0.74	3.74 ± 1.33	5.06 ± 1.37
Putamen	5.68 ± 1.89	2.87 ± 1.00	4.54 ± 1.69	5.64 ± 1.84

were processed in Microsoft Excel (Microsoft, Redmond, WA).

RESULTS

Average regional binding potential values for the four methods are given in Table 1. The traditional ROI-based analysis yielded high binding potential values for the putamen and the caudate nucleus and much lower in the extrastriatal regions. This is in good agreement with previous studies (Farde *et al.*, 1997; Okubo *et al.*, 1999; Olsson *et al.*, 1999; Olsson and Farde, 2001). It must be noted that the values for the striatum are underestimated since the TAC of striatum did not reach peak equilibrium during the time-span of data acquisition (Olsson *et al.*, 1999). The values are, however, useful for the cross validation purposes of the present comparative study.

In the pixel-based analysis the resulting parametric image (Figs. 7a and 8a) is of the same anatomical resolution as the input PET image. The image is heterogeneous due to missing pixels ("black holes"), particularly in regions of high receptor density. These missing pixels represent completely noise-corrupted locations and sudden jumps in the estimated BP values. For each region the values are unanimously lower than the corresponding ROI-based values. According to the regression plot (Fig. 5) they are only about half as high as those of the ROI-based analysis.

In general the results of the 2DTI and 3D wavelet-based analyses (Table 1; Figs. 5, 6, 7b, 7c, 8b, 8c, and 9) were in better agreement with those of the traditional ROI-based method. The regression analysis showed that the estimated regional BP values were about 78% (2DTI) and 100% (3-D) of those with the ROI-based approach (Fig. 5). Figure 6 displays the estimated BP with the three test methods for the nine highest receptor-density anatomical regions in percentage of the BP obtained with the ROI-based method. The values shown are mean and standard deviation for the 10 individuals tested.

The parametric images (Figs. 7b and 7c) obtained by the wavelet approaches show the spatial distribution of binding potential. The resolution is somewhat lower when compared to that of the input image. The parametric maps based on the 3-DWT-aided analysis showed more homogeneous patterns (especially in the axial direction) than those coming from calculations with the plane-by-plane 2-DTI wavelet transform (Figs. 8b and 8c).

DISCUSSION

Both clinical and nonclinical oriented research on neurotransmission has a need for accurate and precise quantification of neuroreceptor binding over a wide density range using PET *in vivo*. High levels of noise in PET images, however, pose a limitation when attempting to create detailed parametric images. Wavelet filters offer a promising way around this problem by differentiating the signal and noise components of the image. A through assessment of the performance of a wavelet-aided parameter estimation procedure should be performed on a dataset containing signals of a broad spectrum of intensities. For this reason [^{11}C]FLB 457 is a good basis for a cross-validation approach as it is able to detect signals from a range of regions with a 100-fold difference in dopamine D_2-receptor density. The results show that it is possible to overcome the effects of noise by the use of the wavelet transform in the parameter estimation procedure.

The noise of the TACs representing single voxels results in a general underestimation of BP when applying a linear graphical pixel-based approach. This observation is consistent with previous findings using the radioligand [^{11}C]WAY 100635 and [^{11}C]NNC 112 (Slifstein and Laruelle, 2000). However, considering the high correlation between the ROI-based and pixel-

based methods ($R^2 = 0.992$) it should be feasible to correct the results of pixel-based analysis by a factor (approximately 2,05 for [^{11}C]FLB 457). Unfortunately voxels in low-receptor density regions were severely affected by noise (see leftmost regions in Fig. 6). It is thus not likely that a corrected pixel-based approach can be used for such regions.

One of the frequently utilised radioligands for testing algorithms in a pixel-by-pixel manner is [^{11}C]raclopride. It has been shown that the average regional values of pixel-based analysis using [^{11}C]raclopride are in good agreement with the results obtained by the analysis of the same regions with the ROI-based approach (Gunn *et al.*, 1997). Therefore, in our view, [^{11}C]raclopride alone is not sufficient for the validation of parameter estimation techniques as the noise-sensitivity of the method may remain unexplored. Although Gunn's method is a highly capable technique, our method of choice was Logan's reference region based graphical analysis as it can be used in both "normal space" methods (ROI-based, simple pixel-based) and "wavelet space" methods. On the other hand, Gunn's method is not applicable in the presented way of wavelet-based analysis due to its non-linear nature. Dealing with a large amount of data, it is also important that the linear graphical method is much faster computationally than Gunn's more complicated method. Neither this nor other additional "normal space" approaches were included as the aim was to assess the capability of the wavelet-aided framework to decrease the noise-sensitivity of a parameter estimation procedure.

Two wavelet approaches were applied. In both approach the wavelet transform is applied spatially not on the time-activity curves of individual pixels as in other studies in the literature (Millet *et al.*, 2000a, 2000b). The reason for this is that noise in 4-D PET images is spatially correlated, thus it is less likely to be eliminated if it is only dealt with in the temporal domain. Besides wavelets do not seem to be an optimal functional base for PET kinetic curves. The most important difference between the two approaches used in this study is whether the wavelet filtering is applied two dimensionally to each slice of the volume or three dimensionally to the whole volume. The other difference was the translation-invariant property of the 2-D approach. The three-dimensional wavelet filtering (3-DWT) was superior to the two-dimensional (2-DWT) approach and the BP was in close agreement with the traditional ROI-based analysis. Translation-invariance cannot account for the systematic and big differences that we observed between the results of the 2-DTI and 3-D methods. This leads to the conclusion that the dimensionality of the filter may have a significant impact on the quality of signal recovery for these types of images.

The performance of the 3-DWT-aided analysis suggests that using this approach a separation of signal and noise and hence a precise estimation of BP can be achieved because it can more accurately detect and represent the information content of the original image regarding the spatial patterns of signal and noise. The accuracy was not impaired even in regions with low receptor-density, i.e., high relative noise levels (Fig. 6). The highest deviations from the reference values were observed in case of the smallest region studied (the substantia nigra). A likely explanation is that too few voxels were averaged to achieve optimal noise reduction even for the ROI-based approach. However, given the accuracy of all other regions the wavelet-based approach should not have been affected, thus providing more accurate estimates. In conclusion the wavelet-aided parameter estimation is an anatomically unbiased procedure for regions with a 100-fold difference in density.

Challenging aspects of the wavelet-based analysis include the possibly time-consuming determination of the best settings for the wavelet transform and the lowered resolution of the resulting parametric images. It should be noted, however, that the maximum level to which wavelets can determine the position *and* the frequency composition of a certain feature of the signal simultaneously is limited by the Gabor uncertainty principle, which is the analogue of Heisenberg's principle in the field of information theory (Gabor, 1946). Whether the resolution of our parametric maps represents this maximum level or the sharpness can be improved is the focus of ongoing developments. As part of that, it is also going to be addressed if the wavelet-filtering parameters are specific with regard to [^{11}C]FLB 457.

Noise was the major factor explaining the differences between the examined methods. The noise in PET images is of complex nature (Pajevic *et al.*, 1998; Turkheimer *et al.*, 1999; Abi-Dargham *et al.*, 2000; Millet *et al.*, 2000b). Individual time frames of such a study can be characterised by low spatial signal-to-noise ratio. Because of the way the reconstruction is usually performed (filtered back-projection), the Gaussian white noise of the individual detection channels becomes correlated in the final image. This correlated distortion of pixel values by relatively high levels of noise cannot be dealt with by the independent analysis of individual TACs, multiple pixel locations must be included in any denoising scheme. Presumably no smaller neighbourhoods of pixels can be analysed independently than the radius of effect of correlation.

In the ROI-based analysis, the problem of noise is reduced through the use of the average value of all pixels representing a certain brain region. In a sense, this might be viewed as "structure-based" filtering of noise. This approach is sufficient for regions with a homogenous distribution of receptors. However, neuroreceptors may be heterogeneously distributed within a

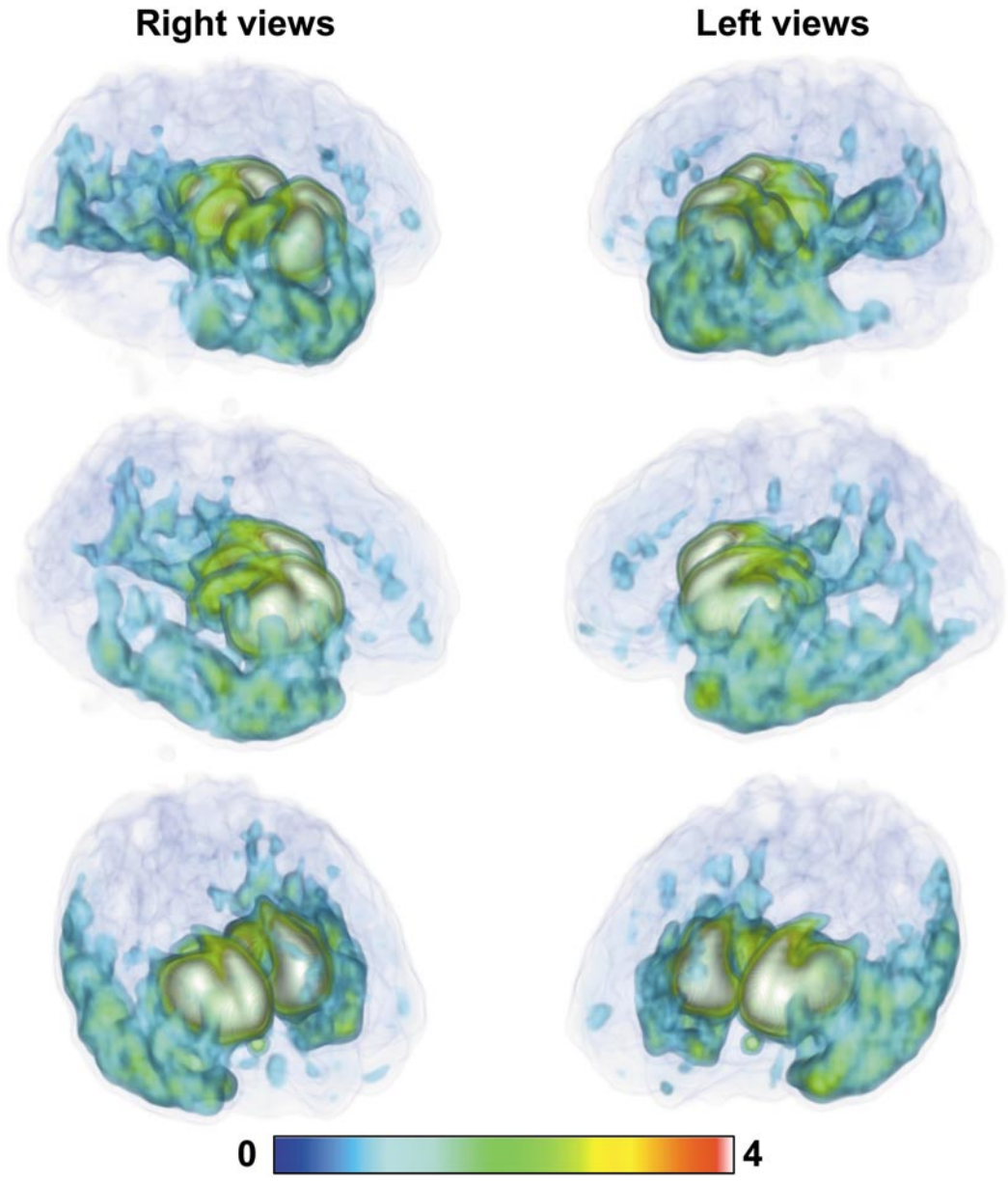

FIG. 9. Volume rendering of dopamine D_2-receptor binding potential created with 3-D wavelet-aided parametric imaging. Left column: right side views; right colum: left side views. First row: posterolateral views; second row: lateral views; third row: anterolateral views. Lowest binding potential regions are completely or almost completely transparent. Besides, for ease of visualization, only certain ranges of binding potential are set to partially opaque, all other values were assigned complete transparency. Visible ranges: around 0.1, transparent blue (majority of the cortex, especially the occipital, the parietal and the frontal cortices); around 0.7, cyan (the temporal cortex, the anterior cingulate cortex, outer parts of the thalamus and the hypophysis); around 1.5, green (inferior, internal parts of the temporal cortex, intermediate boundaries of thalamus, internal parts of the hypophysis); 3.0 and up, yellow, red, white (internal parts of the thalamus, the striatum).

region and information regarding subregional differences may consequently be lost. Simple averaging may also lead to false results if the area of the region is so small that the effect of correlated noise cannot be overcome (possible scenario in case of substantia nigra in the present study).

Another issue regarding noise is the AUC thresholding used to “delete” locations containing noise or no receptors. In this study the criterion was realized using the mean AUC of the reference region. For situations where no reference region is available the criterion could be generalized by for instance using the AUC of the blood or white matter, i.e., any location that has an equal or smaller AUC than one containing receptors. At first glance, the problem seems to be that by this criterion the analysis would

include locations that are devoid of receptors, but have some (interstitial) ligand accumulation. However, if the analytic procedure is good then it will produce near-zero BP for these locations so the final map could be correct. In different words, the AUC thresholding is only doing part of the job of "deleting" noise coefficients; the rest of those are in fact handled by the estimation procedure itself.

Parametric images with accurate values can be utilised in a number of applications. Among others, in contrast with simple regional values obtained they can be used in a statistical framework like SPM or GLM to compare subregional differences in receptor kinetics between different healthy or diseased populations (Friston *et al.*, 1994; Ledberg *et al.*, 1998; Turkheimer *et al.*, 2000b). Besides, both cognitive and neuropsychiatric research can benefit from brain-activation-study-like applications where the aim is to map, in again a statistical framework, subregional changes of binding potential due to drug or cognitive challenge.

In sum, the usefulness of the wavelet filtering lies in being able to suppress noise by averaging over large spatial scales in a fashion that is similar to the ROI-based analyses. At the same time higher spatial frequency information is preserved in the coefficients corresponding to the detail. In short, the wavelet technique allows for the benefits of the ROI approach but does not impose prior assumptions on the exact anatomy of radioligand or receptor distribution. As such it represents a voxel-based approach that has the benefits of noise robustness usually associated with ROI approaches. The present results lead to the conclusion that the combination of three-dimensional spatial wavelet filtering with existing parameter estimation procedures enables us to obtain detailed, accurate maps of radioligand binding parameters.

ACKNOWLEDGMENTS

The authors express their gratitude to Dr. Karl Friston and members of the Hungarian Academy of Sciences' Analogical and Neural Computing Systems Laboratory. The Support by the Science Council of Sweden is acknowledged. Zsolt Cselényi has been a recipient of a stipend from the Swedish Institute during his leave from the Department of Neurology, Debrecen University, Hungary.

REFERENCES

Abadie, P., Baron, J. C., Bisserbe, J. C., Boulenger, J. P., Rioux, P., Travere, J. M., Barre, L., Petit-Taboue, M. C., and Zarifian, E. 1992. Central benzodiazepine receptors in human brain: Estimation of regional Bmax and KD values with positron emission tomography. *Eur. J. Pharmacol.* **213:** 107–115.

Abi-Dargham, A., Martinez, D., Mawlawi, O., Simpson, N., Hwang, D. R., Slifstein, M., Anjilvel, S., Pidcock, J., Guo, N. N., Lombardo, I., Mann, J. J., Van Heertum, R., Foged, C., Halldin, C., and Laruelle, M. 2000. Measurement of striatal and extrastriatal dopamine D1 receptor binding potential with [11C]NNC 112 in humans: Validation and reproducibility. *J. Cereb. Blood Flow Metab.* **20:** 225–243.

Battle, G. 1987. A block spin construction of ondolettes. Part I: Lemarie functions. *Commun. Math. Phys.* **110:** 601–615.

Bergström, M., Boethius, J., Eriksson, L., Greitz, T., Ribbe, T., and Widen, L. 1981. Head fixation device for reproducible position alignment in transmission CT and positron emission tomography. *J. Comput. Assist. Tomogr.* **5:** 136–141.

Blomqvist, G. 1991. Kinetic analysis. *Wien Klin. Wochenschr.* **103:** 451–457.

Blomqvist, G., Pauli, S., Farde, L., Eriksson, L., Persson, A., and Halldin, C. 1990. Maps of receptor binding parameters in the human brain—A kinetic analysis of PET measurements. *Eur. J. Nucl. Med.* **16:** 257–265.

Daubechies, I. 1992. *Ten Lectures on Wavelets*. Society for Industrial and Applied Mathematics, Philadelphia, PA.

Drevets, W. C., Frank, E., Price, J. C., Kupfer, D. J., Holt, D., Greer, P. J., Huang, Y., Gautier, C., and Mathis, C. 1999. PET imaging of serotonin 1A receptor binding in depression. *Biol. Psychiatry* **46:** 1375–1387.

Farde, L., Eriksson, L., Blomquist, G., and Halldin, C. 1989. Kinetic analysis of central [11C]raclopride binding to D2-dopamine receptors studied by PET—A comparison to the equilibrium analysis. *J. Cereb. Blood Flow Metab.* **9:** 696–708.

Farde, L., Hall, H., Pauli, S., and Halldin, C. 1995. Variability in D2-dopamine receptor density and affinity: A PET study with [11C]raclopride in man. *Synapse* **20:** 200–208.

Farde, L., Suhara, T., Nyberg, S., Karlsson, P., Nakashima, Y., Hietala, J., and Halldin, C. 1997. A PET-study of [11C]FLB 457 binding to extrastriatal D2-dopamine receptors in healthy subjects and antipsychotic drug-treated patients. *Psychopharmacology (Berlin)* **133:** 396–404.

Frey, K. A., Holthoff, V. A., Koeppe, R. A., Jewett, D. M., Kilbourn, M. R., and Kuhl, D. E. 1991. Parametric *in vivo* imaging of benzodiazepine receptor distribution in human brain. *Ann. Neurol.* **30:** 663–672.

Friston, K. J., Worsley, K. J., Frackowiak, R. S. J., Mazziotta, J. C., and Evans, A. C. 1994. Assessing the significance of focal activations using their spatial extent. *Hum. Brain Mapp.* **1:** 214–220.

Gabor, D. 1946. Theory of communication. *Proc. Inst. Electr. Eng.* **93:** 429–457.

Gunn, R. N., Lammertsma, A. A., Hume, S. P., and Cunningham, V. J. 1997. Parametric imaging of ligand-receptor binding in PET using a simplified reference region model. *Neuroimage* **6:** 279–287.

Halldin, C., Farde, L., Hogberg, T., Mohell, N., Hall, H., Suhara, T., Karlsson, P., Nakashima, Y., and Swahn, C. G. 1995. Carbon-11-FLB 457: A radioligand for extrastriatal D2 dopamine receptors. *J. Nucl. Med.* **36:** 1275–1281.

Ito, H., Nyberg, S., Halldin, C., Lundkvist, C., and Farde, L. 1998. PET imaging of central 5-HT2A receptors with carbon-11-MDL 100,907. *J. Nucl. Med.* **39:** 208–214.

Kaasinen, V., Nagren, K., Hietala, J., Farde, L., and Rinne, J. O. 2001. Sex differences in extrastriatal dopamine d(2)-like receptors in the human brain. *Am. J. Psychiatry* **158:** 308–311.

Koeppe, R. A., Frey, K. A., Vander Borght, T. M., Karlamangla, A., Jewett, D. M., Lee, L. C., Kilbourn, M. R., and Kuhl, D. E. 1996. Kinetic evaluation of [11C]dihydrotetrabenazine by dynamic PET: Measurement of vesicular monoamine transporter. *J. Cereb. Blood Flow Metab.* **16:** 1288–1299.

Ledberg, A., Akerman, S., and Roland, P. E. 1998. Estimation of the probabilities of 3D clusters in functional brain images. *Neuroimage* **8:** 113–128.

Lemarie, P. G. 1988. Ondolettes a localization exponentielles. *J. Math. Pures Appl.* **67:** 227–236.

Logan, J., Fowler, J. S., Volkow, N. D., Wang, G. J., Ding, Y. S., and Alexoff, D. L. 1996. Distribution volume ratios without blood sampling from graphical analysis of PET data. *J. Cereb. Blood Flow Metab.* **16:** 834–840.

Madar, I., Lever, J. R., Kinter, C. M., Scheffel, U., Ravert, H. T., Musachio, J. L., Mathews, W. B., Dannals, R. F., and Frost, J. J. 1996. Imaging of delta opioid receptors in human brain by N1′-([11C]methyl)naltrindole and PET. *Synapse* **24:** 19–28.

Mallat, S. G. 1989. A theory of multiresolution signal decomposition: the wavelet representation. *IEEE Trans. Pattern Anal. Machine Intell.* **11:** 673–693.

Meyer, Y. 1992. *Wavelets and Operators*. Cambridge Univ. Press.

Millet, P., Graf, C., Buck, A., Walder, B., Westera, G., Broggini, C., Arigoni, M., Slosman, D., Bouras, C., and Ibanez, V. 2000a. Similarity and robustness of PET and SPECT binding parameters for benzodiazepine receptors. *J. Cereb. Blood Flow Metab.* **20:** 1587–1603.

Millet, P., Ibanez, V., Delforge, J., Pappata, S., and Guimon, J. 2000b. Wavelet analysis of dynamic PET data: Application to the parametric imaging of benzodiazepine receptor concentration. *Neuroimage* **11:** 458–472.

Okubo, Y., Olsson, H., Ito, H., Lofti, M., Suhara, T., Halldin, C., and Farde, L. 1999. PET mapping of extrastriatal D2-like dopamine receptors in the human brain using an anatomic standardization technique and [11C]FLB 457. *Neuroimage* **10:** 666–674.

Olsson, H., and Farde, L. 2001. Potentials and pitfalls using high affinity radioligands in pet and spet determinations on regional drug induced d2 receptor occupancy—A simulation study based on experimental data. *Neuroimage* **14:** 936–945.

Olsson, H., Halldin, C., Swahn, C. G., and Farde, L. 1999. Quantification of [11C]FLB 457 binding to extrastriatal dopamine receptors in the human brain. *J. Cereb. Blood Flow Metab.* **19:** 1164–1173.

Pajevic, S., Daube-Witherspoon, M. E., Bacharach, S. L., and Carson, R. E. 1998. Noise characteristics of 3-D and 2-D PET images. *IEEE Trans. Med. Imag.* **17:** 9–23.

Roland, P. E., Graufelds, C. J., Wåhlin, J., Ingelman, L., Andersson, M., Ledberg, A., Pedersen, J., Åkerman, S., Dabringhaus, A., and Zilles, K. 1994. Human brain atlas: For high-resolution functional and anatomical mapping. *Hum. Brain Mapp.* **1:** 173–184.

Slifstein, M., and Laruelle, M. 2000. Effects of statistical noise on graphic analysis of PET neuroreceptor studies. *J. Nucl. Med.* **41:** 2083–2088.

Smith, G. S., Price, J. C., Lopresti, B. J., Huang, Y., Simpson, N., Holt, D., Mason, N. S., Meltzer, C. C., Sweet, R. A., Nichols, T., Sashin, D., and Mathis, C. A. 1998. Test-retest variability of serotonin 5-HT2A receptor binding measured with positron emission tomography and [18F]altanserin in the human brain. *Synapse* **30:** 380–392.

Suhara, T., Yasuno, F., Sudo, Y., Yamamoto, M., Inoue, M., Okubo, Y., and Suzuki, K. 2001. Dopamine D2 receptors in the insular cortex and the personality trait of novelty seeking. *Neuroimage* **13:** 891–895.

Turkheimer, F. E., Banati, R. B., Visvikis, D., Aston, J. A., Gunn, R. N., and Cunningham, V. J. 2000a. Modeling dynamic PET-SPECT studies in the wavelet domain. *J. Cereb. Blood Flow Metab.* **20:** 879–893.

Turkheimer, F. E., Brett, M., Aston, J. A., Leff, A. P., Sargent, P. A., Wise, R. J., Grasby, P. M., and Cunningham, V. J. 2000b. Statistical modeling of positron emission tomography images in wavelet space. *J. Cereb. Blood Flow Metab.* **20:** 1610–1618.

Turkheimer, F. E., Brett, M., Visvikis, D., and Cunningham, V. J. 1999. Multiresolution analysis of emission tomography images in the wavelet domain. *J. Cereb. Blood Flow Metab.* **19:** 1189–1208.

Unser, M., Thevenaz, P., Lee, C., and Ruttiman, U. E. 1995. Registration and statistical analysis of PET images using the wavelet transform. *IEEE Eng. Med. Biol. Mag.* **14:** 603–611.

Wienhard, K., Dahlbom, M., Eriksson, L., Michel, C., Bruckbauer, T., Pietrzyk, U., and Heiss, W. D. 1994. The ECAT EXACT HR: Performance of a new high resolution positron scanner. *J. Comput. Assist. Tomogr.* **18:** 110–118.

Zubieta, J. K., Koeppe, R. A., Mulholland, G. K., Kuhl, D. E., and Frey, K. A. 1998. Quantification of muscarinic cholinergic receptors with [11C]NMPB and positron emission tomography: Method development and differentiation of tracer delivery from receptor binding. *J. Cereb. Blood Flow Metab.* **18:** 619–631.